Hanbo Jiang
Department of Mechanical and Aerospace Engineering,
The Hong Kong University of Science and Technology,
Kowloon, Hong Kong, China
e-mail: hb.jiang@connect.ust.hk

Xun Huang[1]
State Key Laboratory of Turbulence and Complex System,
Department of Aeronautics and Astronautics,
College of Engineering, Peking University,
Beijing 100871, China;
Department of Mechanical and Aerospace Engineering,
The Hong Kong University of Science and Technology,
Kowloon, Hong Kong, China
e-mails: huangxun@pku.edu.cn;
huangxun@ust.hk

Tonal Fan-Noise Radiation From Aero-Engine Bypass With Serrated End Treatments

Chevrons, which are also known as serrations, are initially developed to suppress jet noise radiating from aero-engine nozzles. The associated fluid mechanics are already well known. Compared with jet noise, turbomachinery fan noise has become relatively more important along with the ever-increasing bypass ratio. However, it is still unclear whether the trailing-edge chevrons on the bypass duct would attenuate fan noise and, if the answer is yes, what is the associated mechanism. In this work, we first use a theoretical model based on the Wiener–Hopf method to rapidly conduct parametric studies across a number of different setups. The results from such a theoretical model suggest that the chevrons are also effective in the reduction of fan noise scattering. Next, we perform high-fidelity computational fluid and acoustic simulations for a realistic aero-engine with some representative setups, and the results further confirm the effectiveness of chevrons. Both analytical and numerical results show the associated noise control mechanism, that is, chevrons would induce acoustic mode conversion (especially from low modes to high modes), which shall further result in evanescent waves in the radial direction and the final noise reduction at various radiation angles. The findings may find applications in the next-generation low-noise aero-engine design. [DOI: 10.1115/1.4043882]

1 Introduction

The development of high bypass ratio turbofan engines has led to relatively more prominent fan noise radiating from turbomachinery assemblies, which calls for noise control studies to meet airworthiness certifications [1]. In addition to liner technologies [2–6], chevrons have been proposed especially for the noise reduction from high-speed jet flows. The associated fluid physics is already well known, that is, chevrons would enhance flow mixing and modify large-scale turbulent flow structures to reduce the jet core and eventually lead to decreased aerodynamic noise radiation [7,8]. Chevrons can also be installed on the trailing edge of a bypass duct (such as those on the engines for the new Boeing 787, 747-8X, and 737MAX) and, to the best of the authors' knowledge, it is still not clear whether chevrons could help to control fan noise radiation, which would become relatively more serious for next-generation aero-engines and future full electric engines (where a high-speed jet flow from the combustor would be even absent). The current paper aims to answer this question by (1) first using a theoretical model to rapidly examine the noise control effects of chevrons in a number of different setups, (2) then using high-fidelity computational fluid and acoustic simulation solvers to confirm the control effects for a realistic aero-engine setup, and (3) finally proposing the possible control mechanisms, which would constitute the main contributions of this work.

Chevron, which is also known as serrations, has a presumed connection to the silent flying capabilities of owls [9]. The recent studies of leading-edge serrations [10,11] and trailing-edge serrations [9,10,12] have identified two noise reduction mechanisms. One is the destructive multiple scattering. The other is the induced high modes that could become evanescent in the radial direction. However, the chevron technology used for aero-engine jet noise has presumably followed a different control mechanism, which is not surprising since the jet noise would certainly have different flow-induced noise mechanisms from those of the aerofoil noise problems. Numerical and experimental studies [13–16] have revealed that jet noise reduction is achieved through the enhancement of turbulent mixing and minimization of jet potential core. However, other than high-speed jet flows, rotor-stator turbomachinery assemblies are also one of the dominant noise sources [6,17], and the associated fan noise is the combination of various spinning modes propagating inside and scattering from a cylindrical duct. Theoretically, the interaction between fan noise and the enclosing duct and the interaction between incident (Tollmien–Schlichting or sound pressure) waves and an aerofoil [9,18] are to some extend similar, which motivates us to study the possible noise control effects of serrations for fan noise by essentially following the theoretical methods used for aerofoils.

On the other hand, the acoustic liner remains the most effective noise control method in aero-engine applications [2–5]. Nevertheless, the corresponding control effectiveness may be compromised along with the decreased length of bypass ducts (and the decreased lining surface area). As trailing-edge serration has shown its noise reduction capability for aerofoil applications [9], it would be interesting to examine its fan noise control capabilities for aero-engine applications. To study this effect, the immediate difficulty would come from the nature of fan noise, which consists of multiple tones with hundreds of spinning modes, in the presence of a couple of representative background mean-flow conditions. The corresponding numerical simulations and experimental studies would become prohibitively expensive.

Compared with numerical simulations [19–21] and experimental measurements [22], analytical modeling methods allow rapid predictions with almost negligible cost, which will be especially useful in the preliminary design stage of aero-engines. In particular, a theoretical model based on the so-called Wiener–Hopf method [23] is used in this work by adopting an idealized setup that simplifies an aero-engine with trailing-edge serrations into a semi-infinite duct with serrated ends. The same assumption has been adopted by a series of previous work [2,5,24,25], resulting in several efficient analytic solvers that can be further used for industrial optimization designs [4]. In this work, for each calculation with given chevron profiles, we expect that the analytical model-based solver can produce solutions in a couple of seconds, while for a finite element solver, a dozen of hours is usually required on an ordinary desktop computer. Next, high-fidelity computational simulations

[1]Corresponding author.

Manuscript received November 29, 2018; final manuscript received May 7, 2019; published online May 30, 2019. Assoc. Editor: Li He.

(and experiments) can be performed to further confirm and finalize the design.

The remaining part of this paper is organized as follows. First, Sec. 2 introduces the basic governing equations and boundary conditions of the used analytical model. Section 3 validates the simplified model using finite element analysis and, then, performs parametric studies for a number of different setups. In addition to elucidate the possible control mechanisms, the analytical model enables us to choose shapes and other setups for the following relatively high-fidelity but more expensive computational studies. Next, Sec. 4 performs the computational fluids and acoustic simulations for a realistic aero-engine bypass duct with some representative setups. Section 5 gives a summary of the whole work. Finally, for the completeness of the whole paper, the mathematical derivation of the used model is provided in the Appendix.

2 Theoretical Model

Figure 1 shows the problem setup. The fan noise at a certain frequency can be decomposed to various combinations of radial and azimuthal modes. For example, Fig. 1(*a*) shows a single azimuthal and radial mode at a certain frequency. To enable the following theoretical studies, an idealized setup is sketched in Fig. 1(*b*). The associated sound propagation and scattering from such a setup can be simply described by the following linearized convected wave equations:

$$\left(\frac{\partial}{\partial t}+M_0\frac{\partial}{\partial x}\right)^2\phi-\Delta\phi=0,\quad (x,r)\in\mathfrak{R}_0 \tag{1}$$

$$C_1^2\left(\frac{\partial}{\partial t}+M_1\frac{\partial}{\partial x}\right)^2\phi-\Delta\phi=0,\quad (x,r)\in\mathfrak{R}_1 \tag{2}$$

where ϕ is the acoustic velocity potential, and $\mathfrak{R}_0$ and $\mathfrak{R}_1$ denote the ambient flow region and jet flow region, respectively. The uniform ambient flow is of density ρ_0, velocity $\vec{v}_0$, and speed of sound c_0. The uniform flow inside the bypass duct is of density ρ_1, velocity $\vec{v}_1$, and speed of sound c_1. All variables are nondimensionalized using the duct radius and the free-stream flow density ρ_0, speed of sound c_0 as reference values. Then, the outer radius is normalized to $r=1$. A plug flow model is adopted here, and hence, $\vec{v}_0$ and $\vec{v}_1$ are normalized to M_0 and M_1, respectively.

Following previous studies [2,5], we represent the incident wave and scattering wave by acoustic velocity potentials ϕ_i and ϕ_s, respectively. It is easy to see that both ϕ_i and ϕ_s should satisfy the above convective wave equations in the corresponding regions, respectively. By linear superposition, the total acoustic velocity potential would be

$$\phi(x,r,\theta,t)=\phi_i(x,r,\theta,t)+\phi_s(x,r,\theta,t) \tag{3}$$

Furthermore, ϕ can be simplified to ψ by suppressing the same exponential terms with $\exp(im\theta-i\omega t)$. Then, the incident spinning modal wave ψ_i takes the following analytical form,

$$\psi_i(r,x)=\sum_{m=-\infty}^{\infty}\sum_{n=0}^{\infty}[A_{mn}^{+}e^{i\omega\mu_{mn}^{+}x}+A_{mn}^{-}e^{i\omega\mu_{mn}^{-}x}]\mathrm{J}_m(\alpha_{mn}r) \tag{4}$$

which is the generic solution of the homogeneous Bessel equation by employing separation of variables [2,5], where m denotes the azimuthal mode number and n denotes the radial mode number. A_{mn} is the associated amplitude, $\alpha(m,n)$ is the radial wavenumber, and the superscripts $(\cdot)^{\pm}$ represent the downstream- and upstream-directing waves, respectively. The corresponding nondimensional wavenumbers in the axial direction are

$$\mu_{mn}{}^{\pm}=\frac{\pm\sqrt{1-(1-M_1^2)\alpha_{mn}^2/\omega^2}-M_1}{1-M_1^2} \tag{5}$$

Furthermore, the problem of interest contains various types of boundary conditions, such as the far-field Sommerfeld's radiation condition and the following boundary conditions:

(i) Rigid wall

$$\left.\frac{\partial\psi_i(x,r)}{\partial r}\right|_{r=1}=0,\ \forall x,\quad \left.\frac{\partial\psi_s}{\partial r}(x,r,\theta)\right|_{r=1}=0,\quad \forall x<\chi(\theta) \tag{6}$$

(ii) Pressure continuity

$$\left(-i\omega+M_0\frac{\partial}{\partial x}\right)\psi_s(x,1^+,\theta)=\left(-i\omega+M_1\frac{\partial}{\partial x}\right)(\psi_s(x,1^-,\theta)+\psi_i(x,1^-)),\quad \forall x>\chi(\theta) \tag{7}$$

which ensures pressure continuation across the upper side (1^+) and the lower side (1^-) of the vortex sheets at $r=1$.

(iii) Kinetic displacement

$$\left(\frac{\partial}{\partial t}+M_0\frac{\partial}{\partial x}\right)\xi(x,\theta)=\left.\frac{\partial\psi(x,r,\theta)}{\partial r}\right|_{r=1^+}=\left.\frac{\partial\psi_s(x,r,\theta)}{\partial r}\right|_{r=1^+},\quad \forall x>\chi(\theta) \tag{8}$$

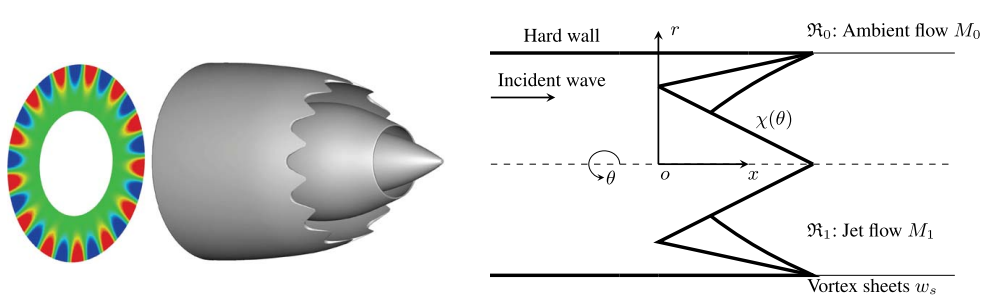

(*a*) (*b*)

Fig. 1 (*a*) An incident fan noise mode and an aero-engine bypass exhaust with a wavy end and (*b*) sketch of the problem. This idealized and nondimensionalized duct geometry consists of a semi-infinite rigid wall and trailing-edge serrations. For simplicity, only three serrations are shown here.

$$\left(\frac{\partial}{\partial t}+M_1\frac{\partial}{\partial x}\right)\xi(x,\theta) = \left.\frac{\partial\psi(x,r,\theta)}{\partial r}\right|_{r=1^-} = \left.\frac{\partial\psi_s(x,r,\theta)}{\partial r}\right|_{r=1^-}, \quad \forall x>\chi(\theta) \tag{9}$$

which means that the displacement speed of the vortex sheets should equal particle velocity of waves. Here, the incident modal wave always satisfies $\partial\psi_i/\partial r \equiv 0$.

Following the derivation from Huang [9], a Wiener–Hopf equation in the matrix form can be obtained. For brevity of the present article, only the most essential derivations would be given in the Appendix, which would enable us to focus on the key engineering topics. In summary, the theoretical model gives the following prediction:

$$\psi_s(x,r,\theta)=\frac{\omega}{2\pi}\int_\Gamma\left(\sum_{\kappa=-\infty}^{+\infty}\beta_s^\kappa(u,r)e^{i\kappa\theta}\right)e^{i\omega ux}\,\mathrm{d}u \tag{10}$$

where

$$\beta_s^\kappa(u,r)=-\frac{i(1-uM_0)\mathrm{H}_{m+\kappa}(\lambda_0\omega r)}{\lambda_0\mathrm{H}'_{m+\kappa}(\lambda_0\omega)}\sum_{\kappa_1=-\infty}^{\infty}F_+^{\kappa_1}(u)L^{\kappa-\kappa_1}(u), \quad r>1 \tag{11}$$

$$\beta_s^\kappa(u,r)=-\frac{i(1-uM_1)\mathrm{J}_{m+\kappa}(\lambda_1\omega r)}{\lambda_1\mathrm{J}'_{m+\kappa}(\lambda_1\omega)}\sum_{\kappa_1=-\infty}^{\infty}F_+^{\kappa_1}(u)L^{\kappa-\kappa_1}(u), \quad r<1 \tag{12}$$

with F^κ analytically representing the noise control effect due to chevrons and the associated detailed definitions can be found in the Appendix.

3 Validations

Before directly using the above theoretical model in our studies, it is mandatory to verify and validate the proposed model first. Hence, a commercial finite/infinite element software ACTRAN® is used in this work to (i) examine the proposed analytic model and (2) further analysis a realistic setup of aero-engine bypass duct with wavy and sawtooth serrations. The first numerical case is performed with the simplified straight duct with sawtooth serrations as shown in Fig. 1(*b*). To validate the analytical model, some probes are set at $(x, r) = (1.5, 1)$, $(2.0, 1)$, and $(2.5, 1)$ to collect acoustic information across the whole θ direction.In addition, near-field comparisons are implemented by comparing sound pressure profiles for a simplified setup with $M_1 = M_0 = 0$. Following the same definitions in Ref. [9], the two key parameters of the chevrons are the period λ_s and root-to-tip length $2h$. Figure 2 shows the sound pressure level (SPL) distributions at those positions from the theoretical model and the numerical solver with SPL defined as follows:

$$\mathrm{SPL}=20\log_{10}\frac{P_{rms}}{2\times10^{-5}} \tag{13}$$

where P_{rms} is the root mean square of sound pressure. It can be seen that the analytical results and the numerical results agree pretty well in most azimuthal angles, which shall be able to help validate the proposed analytic model. Besides, the patterns of the SPL distributions would help to elucidate the possible control effect due to chevrons, and the similar patterns can be observed at the far field as well.

From the perspective of acoustics, far-field performance may be a more important criterion in the evaluation of the noise characteristics of an aero-engine design. The proposed model can be applied for chevrons of various shapes. Figure 3 compares far-field radiation patterns for a cylinder duct with straight, wavy, and sawtooth serrations, respectively. It can be seen that serrations could significantly affect the fan noise radiation patterns from a bypass duct. In particular, compared with Fig. 3(*a*) with a straight duct, the new patterns in Figs. 3(*b*) and 3(*c*) are obviously induced by wavy and sawtooth serrations. As a result, the scattered acoustic field shall consist of multiple circular modes due to serrations. Hence, rather than the absorption of fan noise, chevrons shall enhance mode conversion (from a single one to mixed high and low modes), which would further result in evanescent waves, especially at high modes [5].

Similarly, we found such kind of complex scattering phenomenon due to periodic boundary conditions can be theoretically explained by the famous Tyler–Sofrin selection rule [26]. For the current setups, the effects of wavy and sawtooth serrations are seemingly the same, which is not surprising, because the wavelength of the incident spinning wave is larger than the root-to-tip length of the two types of serrations and, as a result, the difference between these two profiles are relatively small. To better identify the control difference, here we use the so-called total scattering cross section ([9], Eq. (3.2) therein)

$$\sigma=20\log_{10}\int_S\frac{\overline{p_s(\theta,\Theta)}^2}{\overline{p_c(\theta,\Theta)}^2}\,\mathrm{d}S \tag{14}$$

where S is the surface area of the far-field contour as shown in Figs. 3(*a*)–3(*c*) and p_s and p_c represent the far-field pressure with serrations and with straight ends, respectively, where θ is the azimuthal angle and Θ is the radiation angle. The above theoretical model enables us to rapidly evaluate Eq. (14) across a number of parametric combinations, and some results are shown in Fig. 4. It can be seen that sawtooth-shaped chevrons perform slightly better

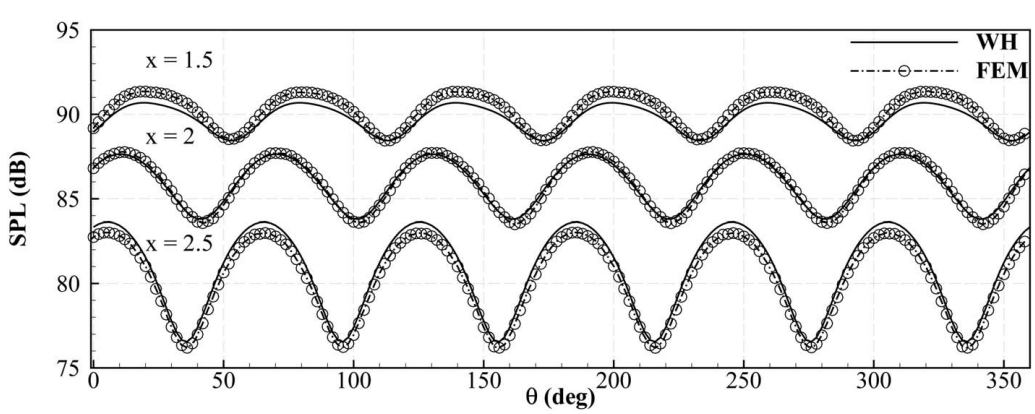

Fig. 2 Near-field sound pressure level distribution for a cylindrical duct with sawtooth serrations of $\lambda = \pi/3$, $2h_s = 0.18$ at $r = 1$ and $x = 1.5, 2.0, 2.5$, where $f = 500$ Hz and mode $(m, n) = (4, 1)$, $M_1 = M_0 = 0$

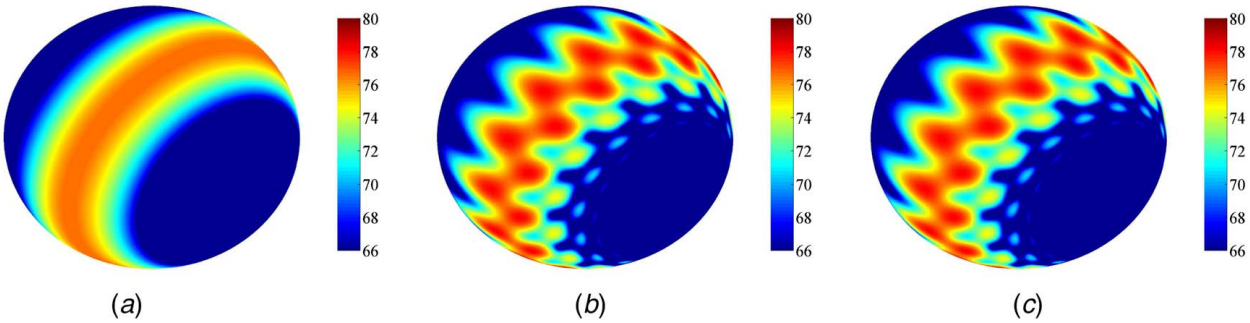

Fig. 3 Sound pressure level contours in the far field. The serrations have a fixed period $\lambda_s = \pi/7$ and a root-to-tip length $2h_s = 0.1$. Other parameters: frequency 900 Hz, mode $(m, n) = (13, 1)$, $M_1 = 0.2$, and $M_0 = 0$. (*a*) Straight edge, (*b*) wavy edge, and (*c*) sawtooth edge.

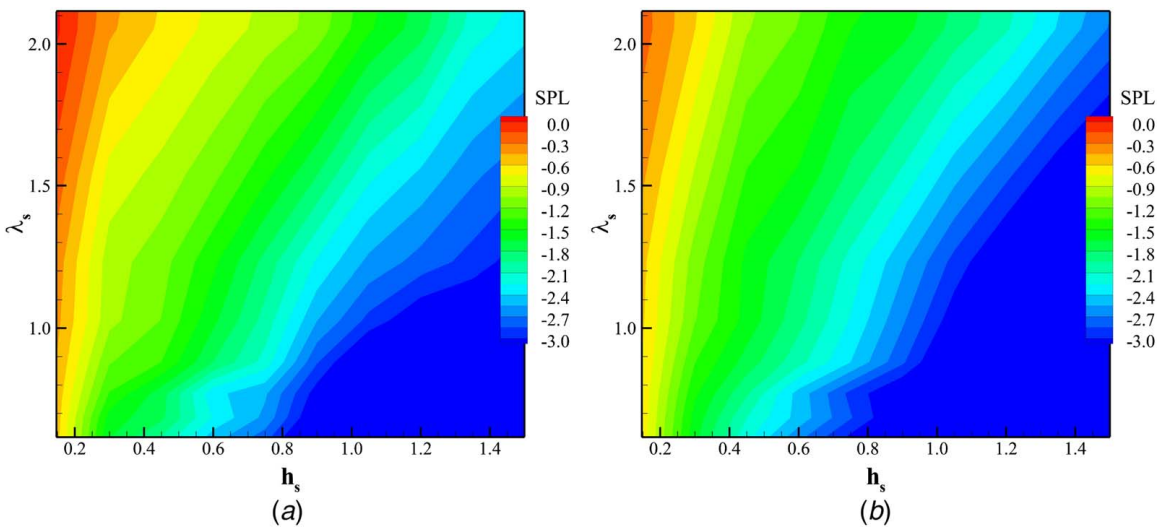

Fig. 4 The contours of the total scattering cross sections σ with respect to different geometrical values of λ_s and h_s, where λ_s and h_s are nondimensionalized by the wavelength of the incident wave, where the incident spinning wave with mode numbers $(m, n) = (8, 0)$, frequency 1000 Hz, $M_0 = 0.0$, and $M_1 = 0.2$. (*a*) Wavy edge and (*b*) sawtooth edge.

than the wavy chevrons for the current setups in terms of the acoustic criterion defined in Eq. (14). Of course, we shall not rule out the possibility that different shapes could achieve better performance at various other setups. Overall, the proposed theoretical model confirms that the chevrons could reduce fan noise through the mode conversion mechanisms and are effective in preliminary parametric studies for idealized setups.

4 Results for a Realistic Aero-Engine Bypass

In the above theoretical studies, we have to adopt an idealized geometrical setup with a simplified plug flow model. In this section, we would further study the control effect for certain realistic aero-engine cases with representative setups. First, we consider the geometry of the aero-engine given previously in Fig. 1(*a*) with an inner radius of 0.55 m and an outer radius of 1.03 m and use a free software GMSH [27] to produce the computational grids. In the near field, the mesh resolution satisfies the required points-per-wavelength [28], while a radiation boundary with infinite elements is used to model sound radiation at the far field. As a result, the computational domain can be decreased into a small region including only the main components (see Fig. 5(*a*)). The total number of elements are more than 4 million.

Figure 5(*a*) shows the basic simulation setups in the simulations where acoustic hard-wall boundary conditions are imposed on the bypass duct walls, and an inlet condition is used to introduce the incident spinning wave as defined in Eq. (4). A high-order infinite elements component is used for the radiation boundary to model sound radiation into the far field and absorb possible sound wave reflections. The background mean flow is first obtained using the open-source solver OPENFOAM (solving the Reynolds-averaged Navier–Stokes equations with the $k-\epsilon$ turbulence model). The time-averaged flow field is then mapped onto the computational acoustic grids. Here, we wish to mention that the computational domain for the background flow simulation is much larger than that for the acoustic simulation. We also wish to mention that the jet flow is excluded in the current study and the associated Mach number is set to zero. However, it shall be quite straightforward to include this flow speed (and even temperature) effect in the late studies. Overall, the current analysis treats the noise and flow field separately, which is a common practice in acoustic studies, and the same procedure can be found in Ref. [29].

As an example, Figs. 6(*a*)–6(*c*) show the sound pressure field of tonal fan noise scattering by the straight edge, the wavy edge, and the sawtooth edge in the presence of a representative background flow (see Fig. 5(*b*)). The two planes shown in Figs. 6(*a*)–6(*c*) are at $(\theta = 0)$ and $(\theta = \pi/2)$, corresponding to the tip and root point of the wavy/sawtooth edge profile, respectively. It can be observed that the total sound field scattering changes in azimuthal direction due to the chevrons, in particular, some small patterns appear on the engine surface with apparently different azimuthal mode number from that of the incident wave. Comparing the results with and without chevrons in Figs. 6(*a*)–6(*c*), we can also find some differences in the sound radiation patterns, which suggests that the

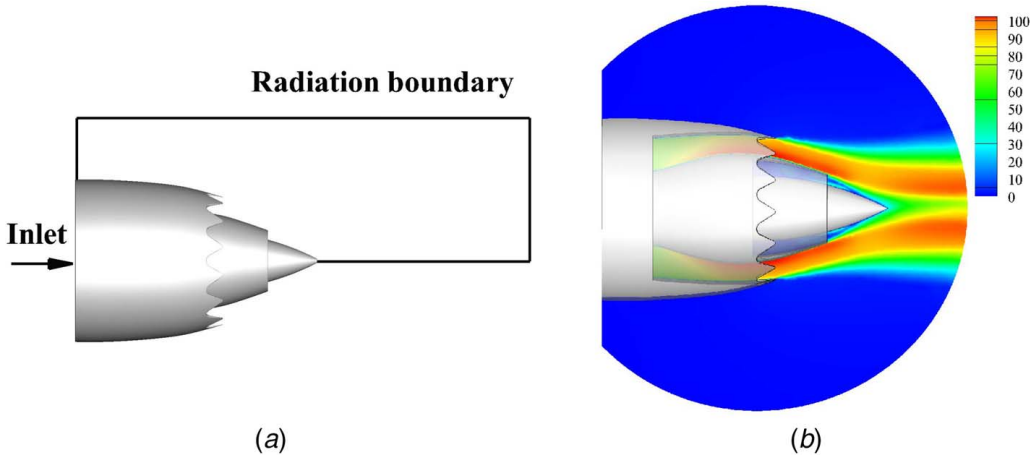

Fig. 5 (*a*) The case setup for acoustic simulations and (*b*) the dimensional axial velocity field (m/s) for the practical aero-engine bypass with a wavy serrated end

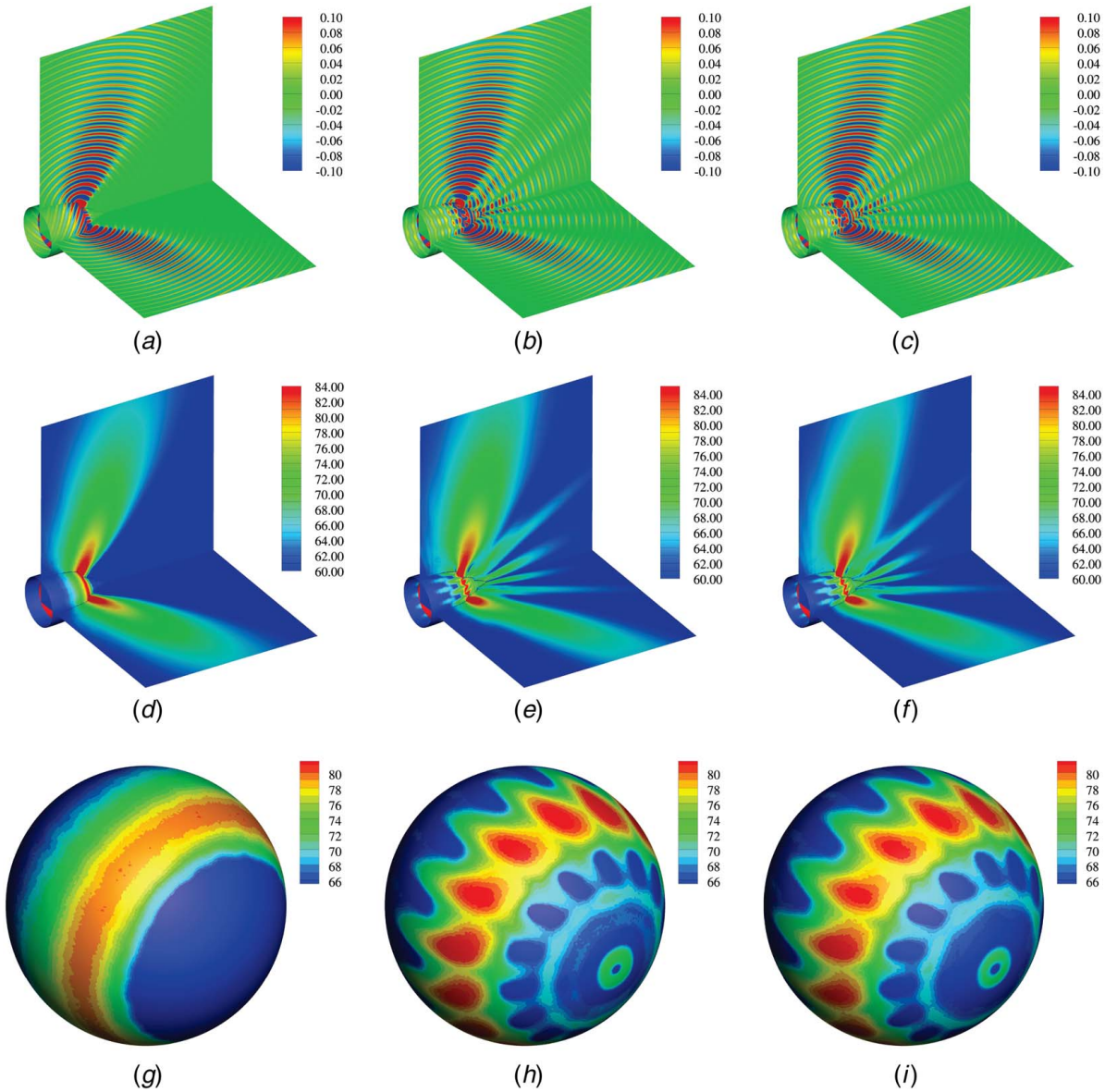

Fig. 6 (*a*)–(*c*) Near-field sound pressure, (*d*)–(*f*) near-field SPL, and (*g*)–(*i*) far-field SPL contours of sound radiation from an aero-engine bypass duct with different edges with incident spinning wave frequency 900 Hz, mode $(m, n) = (13, 1)$, and background mean flow given in Fig. 5(*b*). (*a*), (*d*), and (*g*) Straight edge; (*b*), (*e*), and (*h*) wavy edge; and (*c*), (*f*), and (*i*) sawtooh edge.

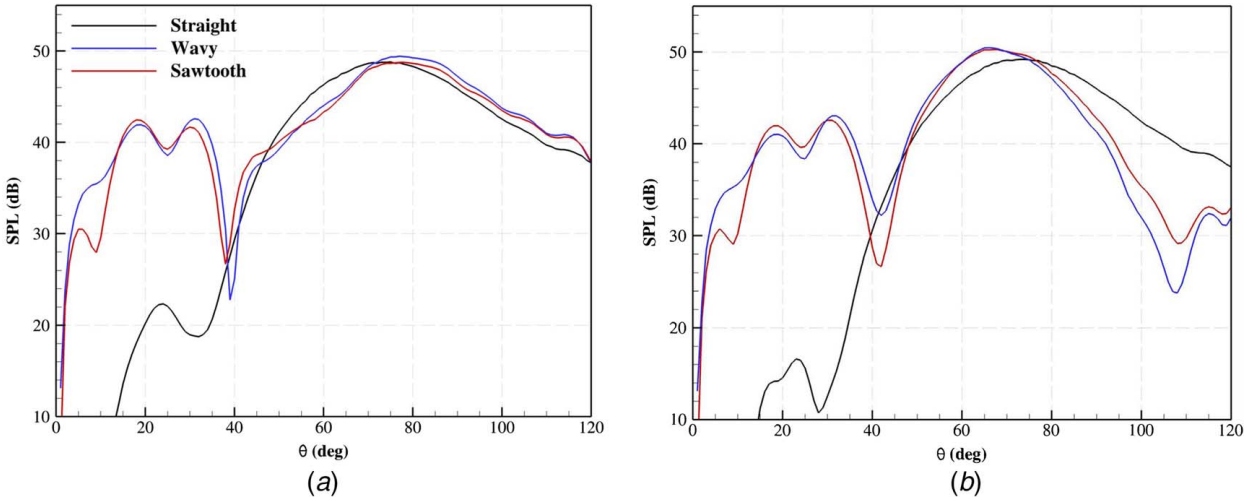

Fig. 7 Far-field directivity patterns in planes of (*a*) top section ($\theta = 0$) and (*b*) root section ($\theta = \pi/2$). Other parameters are the same as Fig. 6.

serrations enhance mode conversion and thus help to redistribute acoustic energy to different radiation angles. Hence, the near-field results should be the combination of the incident waves of the single mode and the scattered waves of discrete radiating modes and a continuum of evanescent modes. The overall pattern is complicated and highly dependent on different setups, which, again, confirms the preliminary design benefit based on theoretical models.

Next, Figs. 6(*c*)–6(*i*) show both the near- and far-field acoustic SPL distributions for tonal fan noise radiation from the aero-engine with straight, wavy, and sawtooth serrations respectively. It can be seen that the patterns shown here are quite similar to those in Fig. 3 especially at the high angles. Hence, we can conclude that it is feasible to use the above theoretical model in the preliminary parametric studies. In addition, compared with the straight edge case in Figs. 6(*d*)–6(*f*) show some new lobes, which should be caused by chevrons and would influence the overall far-field SPL directivities. A similar phenomenon has also been observed by Williamschen and Gabard [29] by directly comparing acoustic power in the far field for aero-engine bypass with and without chevrons. Besides, the far-field SPL results shown in Figs. 6(*d*) and 6(*f*) give a clear impression for the effect of serrations, which, again, indicates that the serrations help to redistribute acoustic energy to different radiation azimuthal angles.

To quantify the performance of wavy and sawtooth serrations, Fig. 7 compares far-field directivity patterns in two planes (as shown in Fig. 6), with the vertical and horizontal planes corresponding to "tip" ($\theta = 0$) and "root" ($\theta = \pi/2$) cross sections, respectively. Compared with the straight edge case, it can be seen that the case with wavy and sawtooth edges make noise slightly increased at the high radiation angles in the "tip" cross section while significantly reduced near the first-dominant lobe, which collectively shifts the lobe into a higher angle. By contrast in the "root" cross section, the first-dominant lobe shifts into a lower angle region with slightly increased amplitudes. Overall, the comparison shown in Fig. 7 for wavy- and sawtooth-shaped serrations suggest that sawtooth-shaped chevrons are more effective at 55–115 deg angle regions, while wavy edges are more effective at 70–120 deg angles, and the significant effects lie in the strong directivity variation to the higher order modes and their phase cancellation. Of course, we must mention that the above discussion is solely from the perspective of acoustics and rules out the possible aerodynamic penalty, which is also a critical issue and should be considered in practical designs.

Last but not least, all above analysis is implemented on a personal computer with an Intel®Xeon CPU E5-1620 v4 @ 3.5 GHz 4 cores. For each complete numerical simulation, the calculation of background flow takes about 30 min, and the acoustic simulation part takes approximately 12 h. In contrast, the simplified analytical model-based solver only takes 5 min for each case. As a result, it should be straightforward to conduct parametric studies by repeating the performance analysis across many working conditions.

5 Summary

The current study focuses on an aero-engine bypass with chevrons, where the incident fan noise consists of discrete tonal spinning modes, which is totally different from jet noise [14]. In this work, we have identified the associated noise control mechanism due to chevrons, first through the studies based on the theoretical Wiener–Hopf based model and then through the studies of high-fidelity computational acoustic studies. In particular, from Figs. 2–7, it can be seen that the incident spinning waves would be scattered into a number of new modes, which further lead to complicated radiation properties, such as main lobe angles and evanescent properties. The superposition of all those scattered modes would cause the redistribution of acoustic power in the far field. Specifically, the sound power is either enhanced or reduced in different radiation angles, and collectively, the mode conversion would lead to an overall noise reduction.

To enable theoretical modeling, a couple of geometrical simplifications and assumptions have been adopted in the theoretical model. As a result, the model would enable rapid predictions and would prove to be very useful especially in preliminary designs. A high-fidelity numerical simulation can then be performed to further confirm the noise control mechanisms (and, of course, to optimize the chevron designs). The results shown in this paper, however, suggest that the analytical model agrees quite well with the numerical solver, although the simplified analytic model excludes the effect of the center body and other geometry variation and the sheared background flows. Overall, both studies based on the theoretical model and numerical simulations confirm that chevrons would be effective in the control of fan noise from a turbofan engine. The same conclusion should be applicable to next-generation turbofan aero-engines with ever-increasing bypass ratio and full electric aero-engines without jet flows.

Acknowledgment

This work is partly supported by National Science Foundation of China (Grants 11772005, 91852201), Ministry of Industry and Information Technology of China (Grant no. MJ-2015-F-012-03),

and the Research Grants Council of the Hong Kong Special Administrative Region (Grant no. 16205317). The numerical investigation is supported by High-performance Computing Platform of Peking University.

Appendix

The following part is the most succinct description of the Wiener–Hopf model for duct fan noise with chevrons. For more detailed explanation, readers of interest can refer to Refs. [2,5,24,25,30].

To solve the problem of interest defined by Eqs. (1) and (2), we first define the Fourier transforms for the velocity potential in the form of

$$\beta_s(u, r, \theta) \triangleq \int_{-\infty}^{+\infty} \psi_s(x, r, \theta) e^{-i\omega u x} \mathrm{d}x \tag{A1}$$

where u is the normalized wavenumber in the axial direction. Then, we can reduce the convected wave equations (Eqs. (1)–(2)) to the following Bessel equations:

$$\frac{1}{r}\frac{\partial}{\partial r}\left(r\frac{\partial \beta_s^\kappa}{\partial r}\right) + \left[\omega^2\lambda_{0,1}^2 - \frac{(m+\kappa)^2}{r^2}\right]\beta_s^\kappa = 0 \tag{A2}$$

where $\lambda_{0,1}^2 = (1 - uM_{0,1})^2 - u^2$, $\lambda_{0,1} = \lambda_{0,1}^+\lambda_{0,1}^-$ with $\lambda_{0,1}^\pm = ((1 - uM_{0,1}) \pm u)^{1/2}$. It can be seen that $\lambda_{0,1}$ is independent of azimuthal modes, and as a result, the branch cuts chosen here are still the same as those in the previous works [24,30].

By taking account of the symmetrical condition and radiation condition together, the solution $\beta_s^k(r, u)$ shall take the following forms:

$$\beta_s^\kappa(u, r) = A^\kappa(u)\mathrm{H}_{m+\kappa}(\lambda_0\omega r), \quad r > 1 \tag{A3}$$

$$\beta_s^\kappa(u, r) = B^\kappa(u)\mathrm{J}_{m+\kappa}(\lambda_1\omega r), \quad r < 1 \tag{A4}$$

where $\mathrm{J}_{m+\kappa}$ and $\mathrm{H}_{m+\kappa}$ are the $(m+\kappa)$th order Bessel function of the first kind and Hankel function, respectively, and $A^\kappa(u)$ and $B^\kappa(u)$ are the associated amplitudes. Hence, one can immediately reach to the important conclusion that the scattering waves would consist of a series of new azimuthal modes $(m+\kappa, \forall\kappa)$ apart from the incident azimuthal mode (m) due to the trailing-edge serrations.

Combining the boundary conditions (6)–(8), we can obtain the expressions of $A^\kappa(u)$ and $B^\kappa(u)$ as follows:

$$A^\kappa(u) = -\frac{i(1 - uM_0)}{\lambda_0\mathrm{H}'_{m+\kappa}(\lambda_0\omega)}\sum_{\kappa_1=-\infty}^{\infty} F_+^{\kappa_1}(u)L^{\kappa-\kappa_1}(u) \tag{A5}$$

$$B^\kappa(u) = -\frac{i(1 - uM_1)}{\lambda_1\mathrm{J}'_{m+\kappa}(\lambda_1\omega)}\sum_{\kappa_1=-\infty}^{\infty} F_+^{\kappa_1}(u)L^{\kappa-\kappa_1}(u) \tag{A6}$$

where

$$F_+(u, \theta) = \int_0^{+\infty} \xi(\hat{x} + \chi(\theta), \theta)e^{-i\omega u\hat{x}}\mathrm{d}\hat{x}, \quad L(u, \theta) = e^{-i\omega u\chi(\theta)}, \quad \hat{x} = x - \chi(\theta) \tag{A7}$$

Here, $\chi(\theta)$ defines the profiles of the trailing-edge serrations (see Fig. 1(*b*)); the relation for vortex sheets $\xi(x, \theta) = 0$ when $x < \chi(\theta)$ is implicitly adopted; and $(\cdot)_+$ denotes the regularity on the lower half u-plane (i.e., R_+, see Fig. 3(*a*) in Ref. [5]). Note that here the superscripts $(\cdot)^\pm$ represent the upper and lower sides in the r direction, while the subscripts $(\cdot)_\pm$ represent the regularity on the R_+ and R_- half planes, respectively.

Following previous works [2,5,9], a special function should be introduced first:

$$\tilde{G}(u, \theta) = \int_{-\infty}^{+\infty}\left(-i\omega + M_0\frac{\partial}{\partial x}\right)\psi_s(x, 1^+, \theta)e^{-i\omega u x}\,\mathrm{d}x - \int_{-\infty}^{+\infty}\left(-i\omega + M_1\frac{\partial}{\partial x}\right)\psi_s(x, 1^-, \theta)e^{-i\omega u x}\,\mathrm{d}x \tag{A8}$$

which is then split into a sum of $\tilde{G}_+(u, \theta)$ and $\tilde{G}_-(u, \theta)$, where

$$\tilde{G}_+ \triangleq \int_{\chi(\theta)}^{+\infty} -i\omega\left(1 - M_1\mu_{mn}^+\right)A_{mn}^+\mathrm{J}_m(\alpha_{mn})e^{i\omega(\mu_{mn}^+ - u)x}\,\mathrm{d}x = G_+(u, \theta)L(u, \theta)$$

with

$$G_+(u, \theta) = \frac{(1 - M_1\mu_{mn}^+)A_{mn}^+\mathrm{J}_m(\alpha_{mn})}{\mu_{mn}^+ - u}e^{i\omega\mu_{mn}^+\chi(\theta)} \tag{A9}$$

Note that Eq. (A9) is obtained by using the pressure continuity condition Eq. (7), far-field Sommerfeld's radiation condition and the definition of the incident wave Eq. (4) together. Then, we have the following relation from Eq. (A8):

$$-i\omega(1 - M_0u)\beta_s(u, 1^+, \theta) + i\omega(1 - M_1u)\beta_s(u, 1^-, \theta) = \tilde{G}_+(u, \theta) + \tilde{G}_-(u, \theta) \tag{A10}$$

Next, by observing the periodicity of $\beta_s(u, r, \theta)$ and $\tilde{G}_\pm(u, \theta)$ in the azimuthal direction, we can apply the Fourier series expansions to Eq. (A10)

$$\omega\sum_{\kappa=-\infty}^{+\infty} K^\kappa(u)\sum_{\kappa_1=-\infty}^{\infty} F_+^{\kappa_1}(u)L^{\kappa-\kappa_1}(u) = \sum_{\kappa=-\infty}^{\infty} G_+^\kappa + \sum_{\kappa=-\infty}^{\infty} G_-^\kappa \tag{A11}$$

with the following important kernel element:

$$K^\kappa(u) = \frac{(1 - uM_1)^2}{\lambda_1}\frac{\mathrm{J}_{m+\kappa}(\lambda_1\omega)}{\mathrm{J}'_{m+\kappa}(\lambda_1\omega)} - \frac{(1 - uM_0)^2}{\lambda_0}\frac{\mathrm{H}_{m+\kappa}(\lambda_0\omega)}{\mathrm{H}'_{m+\kappa}(\lambda_0\omega)} \tag{A12}$$

Next, we have the matrix Wiener–Hopf equations by equating the same κth order terms on the left- and right-hand sides of Eq. (A11),

$$\omega\mathscr{K}(u)\boldsymbol{F}_+(u) = \boldsymbol{G}_+(u) + \boldsymbol{G}_-(u) \tag{A13}$$

where

$$\mathscr{K}(u) = \boldsymbol{L}^{-1}(u)\boldsymbol{K}(u)\boldsymbol{L}(u) \tag{A14}$$

with

$$\boldsymbol{K} = \begin{pmatrix} \ddots & & & & \\ & K^{-1} & & & \\ & & K^0 & & \\ & & & K^1 & \\ & & & & \ddots \end{pmatrix}, \quad \boldsymbol{L} = \begin{pmatrix} \ddots & & & & \\ \cdots & L^0 & L^{-1} & L^{-2} & \cdots \\ \cdots & L^1 & L^0 & L^{-1} & \cdots \\ \cdots & L^2 & L^1 & L^0 & \cdots \\ & & & & \ddots \end{pmatrix}$$

$$\boldsymbol{F}_+ = \begin{pmatrix} \vdots \\ F_+^{-1} \\ F_+^0 \\ F_+^1 \\ \vdots \end{pmatrix}, \quad \boldsymbol{G}_- = \begin{pmatrix} \vdots \\ G_-^{-1} \\ G_-^0 \\ G_-^1 \\ \vdots \end{pmatrix}, \quad \boldsymbol{G}_+ = \begin{pmatrix} \vdots \\ G_+^{-1} \\ G_+^0 \\ G_+^1 \\ \vdots \end{pmatrix} \tag{A15}$$

It can be seen that each item of the above matrices has been defined previously. In the following numerical implementations, the matrices will be first truncated and the possible truncation error has been discussed previously by Liu et al. [2] and Jiang et al. [5]. The

solution is obtained based the on the Wiener–Hopf method, where a matrix kernel function $\mathscr{K}(u)$ is explicitly factorized as $\mathscr{K}(u) = \mathscr{K}_+\mathscr{K}_-$ using the method by Heins [31]. Finally, we have the solution

$$\boldsymbol{F}_+(u) = \omega^{-1}\mathscr{K}_+^{-1}(u)\mathscr{K}_-^{-1}(\mu_{mn}^+)\boldsymbol{G}_+(u) \tag{A16}$$

References

[1] Zhang, X., 2012, "Aircraft Noise and Its Nearfield Propagation Computations," Acta Mech. Sin., **28**(4), pp. 960–977.

[2] Liu, X., Jiang, H., Huang, X., and Chen, S., 2016, "Theoretical Model of Scattering From Flow Ducts With Semi-Infinite Axial Liner Splices," J. Fluid Mech., **786**, pp. 62–83.

[3] Jiang, H., Lau, A., and Huang, X., 2017, "An Efficient Algorithm of Wiener-Hopf Method With Graphics Processing Unit for Duct Acoustics," ASME J. Vib. Acoust., **139**(5), p. 054501.

[4] Jiang, H., Lau, A., and Huang, X., 2018, "Surrogate Model Based Liner Optimization for Aeroengines and Comparison With Finite Elements," ASME J. Vib. Acoust., **140**(3), p. 034501.

[5] Jiang, H., Lau, A., and Huang, X., 2018, "Sound Wave Scattering in a Flow Duct With Azimuthally Non-Uniform Liners," J. Fluid Mech., **839**, pp. 644–662.

[6] Lau, A., Zhong, S., and Huang, X., 2018, "Control-Oriented Methods for Turbomachinery Noise Simulation," ASME J. Turbomach., **140**(1), p. 011001.

[7] Nikam, S., and Sharma, S., 2018, "Effect of a Chevron Nozzle on Noise Radiation From a Compressible Jet," AIAA J., **56**(11), pp. 4361–4378.

[8] Ran, L., Ye, C., Wan, Z., Yang, H., and Sun, D., 2018, "Instability Waves and Low-frequency Noise Radiation in the Subsonic Chevron Jet," Acta Mech. Sin., **34**(3), pp. 421–430.

[9] Huang, X., 2017, "Theoretical Model of Acoustic Scattering From a Flat Plate With Serrations," J. Fluid Mech., **819**, pp. 228–257.

[10] Ayton, L. J., and Kim, J. W., 2018, "An Analytic Solution for the Noise Generated by Gust-Aerofoil Interaction for Plates With Serrated Leading Edges," J. Fluid Mech., **853**, pp. 515–536.

[11] Lyu, B., and Azarpeyvand, M., 2017, "On the Noise Prediction for Serrated Leading Edges," J. Fluid Mech., **826**, pp. 205–234.

[12] Lyu, B., Azarpeyvand, M., and Sinayoko, S., 2016, "Prediction of Noise From Serrated Trailing Edges," J. Fluid Mech., **793**, pp. 556–588.

[13] Tinney, C. E., and Jordan, P., 2008, "The Near Pressure Field of Co-axial Subsonic Jets," J. Fluid Mech., **611**, pp. 175–204.

[14] Xia, H., Tucker, P. G., and Eastwood, S., 2009, "Large-Eddy Simulations of Chevron Jet Flows With Noise Predictions," Int. J. Heat Fluid Flow, **30**(6), pp. 1067–1079.

[15] Tide, P. S., and Srinivasan, K., 2010, "Effect of Chevron Count and Penetration on the Acoustic Characteristics of Chevron Nozzles," Appl. Acoust., **71**(3), pp. 201–220.

[16] Bin, J. U. A., and Hussaini, M. Y., 2010, "Adaptive Mesh Refinement for Chevron Nozzle Jet Flows," Comput. Fluids, **39**(6), pp. 979–993.

[17] He, L., 2010, "Fourier Methods for Turbomachinery Applications," Prog. Aerosp. Sci., **46**(8), pp. 329–341.

[18] Lau, A., and Huang, X., 2018, "The Control of Aerodynamic Sound Due to Boundary Layer Pressure Gust Scattering by Trailing Edge Serrations," J. Sound Vib., **432**, pp. 133–154.

[19] Tyacke, J., Naqavi, I., Wang, Z. N., Tucker, P., and Boehning, P., 2017, "Predictive Large Eddy Simulation for Jet Aeroacoustics-Current Approach and Industrial Application," ASME J. Turbomach., **139**(8), p. 081003.

[20] González, A. S., and Aparicio, J. R. F., 2016, "Turbine Tone Noise Prediction Using a Linearized Computational Fluid Dynamics Solver: Comparison With Measurements," ASME J. Turbomach., **138**(6), p. 061006.

[21] Groeneweg, J. F., and Rice, E., 1987, "Aircraft Turbofan Noise," ASME J. Turbomach., **109**(1), pp. 130–141.

[22] Darvish, M., Frank, S., and Paschereit, C. O., 2015, "Numerical and Experimental Study on the Tonal Noise Generation of a Radial Fan," ASME J. Turbomach., **137**(10), p. 101005.

[23] Noble, B., 1958, *Methods Beaded on the Wiener-Hopf Technique for the Solution of Partial Differential Equations*, Pergamon Press, London.

[24] Munt, R. M., 1977, "The Interaction of Sound With a Subsonic Jet Issuing From a Semi-Infinite Cylindrical Pipe," J. Fluid Mech., **83**, pp. 609–640.

[25] Gabard, G., and Astley, R. J., 2006, "Theoretical Model for Sound Radiation From Annular Jet Pipes: Far- and Near-field Solutions," J. Fluid Mech., **549**, pp. 315–341.

[26] Tyler, J. M., and Sofrin, T. G., 1962, "Axial Flow Compressor Noise Studies," Technical Report No. 620532, SAE Technical Paper.

[27] Geuzaine, C., and Remacle, J. F., 2009, "Gmsh: A 3-D Finite Element Mesh Generator With Built-In Pre-and Post-Processing Facilities," Int. J. Numer. Method Eng., **79**(11), pp. 1309–1331.

[28] Huang, X., Chen, X. X., Ma, Z. K., and Zhang, X., 2008, "Efficient Computation of Spinning Modal Radiation Through An Engine Bypass Duct," AIAA J., **46**(6), pp. 1413–1423.

[29] Williamschen, M., and Gabard, G., 2017, "Diffraction of Tonal Noise by Chevrons in a Turbofan Exhaust," AIAA Paper No. 2017–3032.

[30] Rienstra, S. W., 1984, "Acoustic Radiation From a Semi-infinite Annular Duct in a Uniform Subsonic Mean Flow," J. Sound Vib., **94**(2), pp. 267–288.

[31] Heins, A. E., 1950, "Systems of Wiener–Hopf Equations," Proceedings of the Symposia in Applied Mathematics II, New York, pp. 76–81.